

Inverse asymmetrical ridge taper polarization splitter-rotator covering optical fiber communication band from O to U

Zhanqiang Hui^{1*}, Tianshu Zhang¹, Meizhi Zhang¹, Deng Pan, Dongdong Han, Abdel-Hamid Soliman²

¹ *School of Electronic Engineering, Xi'an University of Posts and Telecommunications, Xi'an, 710121, China*

² *Staffordshire University, Staffordshire, ST4 2DE, UK*

* zhanqianghui@xupt.edu.cn

Abstract

A novel on-chip ultra-broadband polarization splitter-rotator (PSR) based on an inverse asymmetrical ridge taper coupler is proposed by using evanescent coupling between two straight waveguides with gradual ridge widths. The two ridge-widths decrease inversely to realize mode hybridization between fundamental transverse magnetic (TM₀) mode and fundamental transverse electric (TE₀) mode, which effectively expands the bandwidth. The structural parameters are optimized by utilizing the frequency-domain finite-difference and eigenmode expansion method. The results show that efficient polarization splitting and rotating are simultaneously achieved with a broad operating bandwidth from 1250 nm to 1750 nm and a high polarization conversion efficiency of more than 95%. The insertion loss is below 0.05 dB and 0.2 dB over the bandwidth for TE₀ and TM₀, respectively. To the best of our knowledge, the PSR achieves the broadest bandwidth up to 500 nm (covering all the optical fiber communication O-, E-, S-, C-, L-, and U-bands) for the first time.

Keywords: Adiabatic taper, Polarization-selective devices, Silicon-on-insulator (SOI), Conversion efficiency

1 Introduction

In the past decade, photonic integrated devices based on SOI platform have received considerable attention because of their compatibility with the mature complementary metal-oxide-semiconductor (CMOS) technology and large transparent window [1]. However, high birefringence is a serious problem due to the relatively large aspect ratio of SOI waveguides (typically 2:1) and the high-index contrast between the silicon and the surrounding media [2], which usually leads to polarization mode dispersion, polarization crosstalk as well as polarization-dependent loss, and ultimately limits the photonic network system performance [3]. So an important solution of employing an integrating polarization diversity system was put forward to address this issue, which commonly consists of polarization rotator (PR) [4–8], polarization beam splitters (PBS) [9–13], or polarization splitter-rotator (PSR) [14–32]. Among them, PSR has attracted considerable attention due to the excellent ability of performing polarization splitting and rotating simultaneously. It can be regarded as a combination of a PBS and PR, which splits input light with arbitrary polarizations into two orthogonal polarization states spatially and then rotates one of the polarization states by 90° while keeping the other polarization component invariable. Then, only

single polarization state remains in photonic integrated circuits and avoids the various polarization related unfavorable effects.

So far, a series of PSRs based on SOI platform have been reported [14–32]. They can be categorized into two types: mode coupling and mode evolution mechanism. The former consists of optical waveguides with constant cross-sections. Such as using asymmetrical directional coupler (ADC) [14,15], bend waveguide with suitable optical length [16–18], and subwavelength grating structure [19,20]. A high-efficient cross-polarization coupling occurs between two orthogonal polarization modes in different silicon waveguides, which is caused by the phase matching of the two modes originateing from waveguides optical asymmetry in vertical direction. This type of device is compact but usually has tight fabrication tolerance and a smaller operating wavelength range.

On the other hand, mode evolution PSRs have gradual cross-section along transmission direction, which supports mode hybridization in a varied waveguide segment. This type of PSRs commonly has advantages in fabrication tolerance and insertion loss. Nonetheless, it is not easy to meet the phase-matching requirement by reducing the effective refractive index (n_{eff}) difference between TE_0 mode and TM_0 mode in a standard SOI wafer. So an assist high order mode such as TE_1 mode was introduced as a transient state of mode evolution to achieve polarization rotation (i.e. $\text{TM}_0 - \text{TE}_1 - \text{TE}_0$). For example, using adiabatic taper [21–28] or bi-level taper [29,30] as a TM_0 - TE_1 polarization rotator, and using ADC [21–24,29,30], Y-branch [26,31], and multi-mode interferer (MMI) [27,28,32] as TE_1 - TE_0 mode converter realized in series. However, all above mentioned PSRs have their advantages and disadvantages in terms of cost, footprint, and polarization conversion efficiency. Moreover, most of them suffer from a relatively narrow operating bandwidth since the polarization conversion length is sensitive to wavelength. A PSR with broad bandwidth is highly desired especially for ultra-high-speed coherent transceivers and for high-dense on-chip photonic networks.

In this paper, a novel ultra-broadband PSR based on an inverse asymmetrical ridge taper coupler is proposed. Polarization splitting and rotation can be achieved directly without involving the higher-order modes transmission, since inverse gradual ridge waveguides width satisfies phase-matching condition between input port TM_0 mode and cross port TE_0 mode. The simulation results show polarization conversion efficiency higher than 95% and crosstalk lower than -30 dB within the operating wavelength range from 1250 nm to 1750 nm are obtained. It can work over all the optical fiber communication bands and fully meet the requirement of practical WDM applications.

2 Structure design and principle

The cross section, 3D and top views of the proposed PSR device structure are plotted in Fig. 1(a), (b), and (c), respectively. It consists of two asymmetrical ridge silicon taper waveguides coupled to each other based on SOI platform. The thickness of the top silicon layer H_{co} is standard 220 nm with air cladding to maximize vertical optical asymmetry. The two optical waveguides have different ridge and slab widths to satisfy the phase-matching condition for obtaining polarization splitting and

subsequently achieving efficient TM-TE conversion under appropriate coupling. The ridge width of input waveguide W_{t1} is tapered from W_{s1} to 0 along transmission direction, whereas the ridge width of cross port waveguide is continuously widening from 0 to W_{s2} . The slab widths are fixed W_{s1} and W_{s2} , respectively. Ridge heights etch depth H_t are identical for two waveguides, considering the feasibility of fabrication. The rib taper length is L_c , and the gap width of two waveguides is $W_g = 120$ nm considering the limitation of the deep-UV lithography process [29].

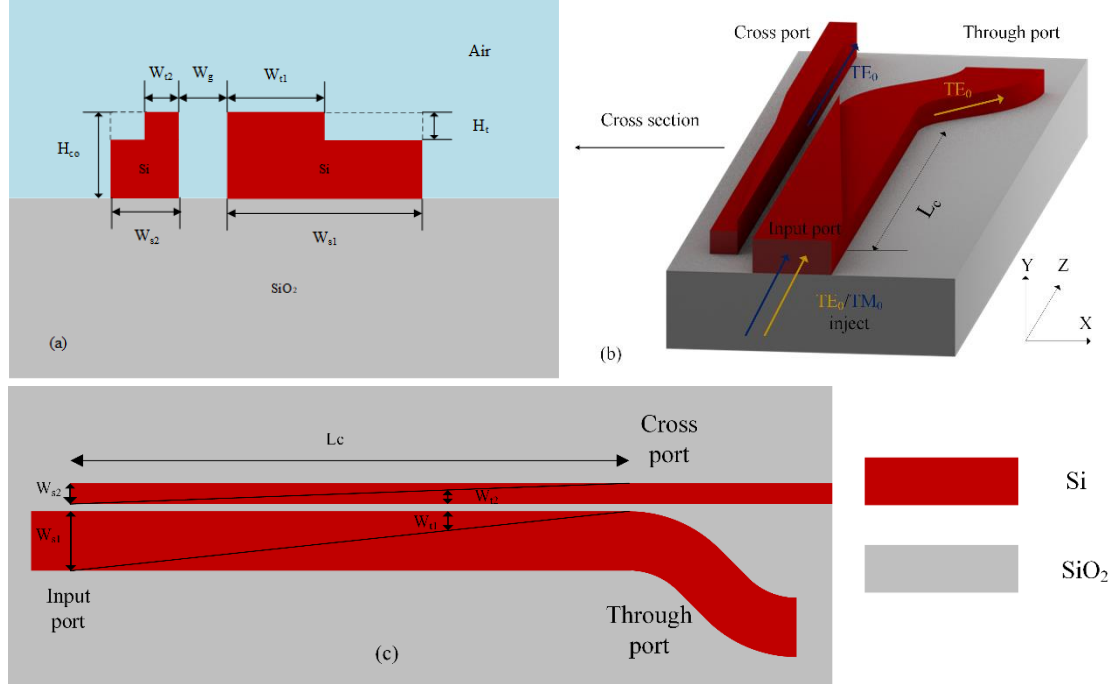


Fig. 1. Schematic structure of proposed inverse asymmetrical ridge taper coupler: (a) Cross section (b) 3D view (c) Top view

In general, the requirement of waveguide is to provide dielectric constant high enough to limit the electromagnetic field of the guided mode near the waveguide structure. If adding an additional waveguide near the initial waveguide, mode coupling will be produced resulting from dielectric perturbation. Therefore, for the guided mode in the input waveguide, when it enters the waveguide region satisfying the coupling conditions, part of its energy will be transferred to another mode due to the evanescent coupling effect. The amplitudes of the coupled modes can be calculated by the coupling mode theory [33], as shown in the following equations :

$$\frac{dA_1}{dz} = -i\kappa A_2(z)e^{i2\delta z} \quad (1)$$

$$\frac{dA_2}{dz} = -i\kappa A_1(z)e^{-i2\delta z} \quad (2)$$

Where A_1 , A_2 are the amplitudes of both modes, 2δ is the phase mismatching defined as difference of the propagation constants of two coupled modes. κ is the coupling coefficient between two modes which can be defined as:

$$\kappa = \frac{\omega}{4} \iint E_1^*(x,y) \cdot \Delta \varepsilon_1(x,y,z) E_2(x,y) dx dy \quad (3)$$

Where E_1 and E_2 are the electric profiles of coupled modes, $\Delta \varepsilon_1$ and $\Delta \varepsilon_2$ are the permittivity perturbation for both waveguides, ω is the angular frequency. Considering the situation of single mode input (i.e., the initial condition is $A_1(0) = A_0$, $A_2(0) = 0$), the solution to the equation (1) can be given by:

$$P_2(z) = |A_2(z)|^2 = A_0^2 \frac{\kappa^2}{\kappa^2 + \delta^2} \sin^2 z \sqrt{\kappa^2 + \delta^2} \quad (4)$$

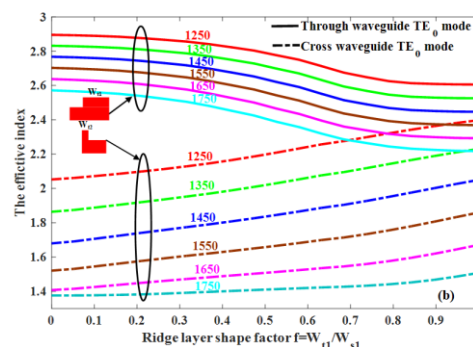
According to (4), complete energy transfer only occurs in a coupling length $L_c = \pi/2\kappa$ with $\delta = 0$, which means the propagation constants of the two modes should be identical.

In PSRs based on mode evolution, β_1 and β_2 are determined by taper structure, which change regularly with z , so δ is variable. For our proposed PSR, which can split input light with arbitrary polarization states into TE_0 and TM_0 spatially and then convert TM_0 to TE_0 . Therefore, for input TM_0 mode, δ should be suppressed to maximum conversion efficiency. In contrast, for input TE_0 mode, the value of δ should be increased in order to avoid mode coupling. Note that it is challenging to eradicate the effective index difference between quasi- TE_0 and quasi- TM_0 mode due to material and fabrication restrictions. The conventional PSR based on mode evolution usually introduces auxiliary higher-order modes to compensate for this defect, so it needs two cascaded mode conversions, which makes the mode conversion loss double and the structure complex. However, in this design, a couple of inverse ridge taper with gradual widths W_{t1} and W_{t2} has been utilized to satisfy the phase-matching condition between the two fundamental modes and realize the mode conversion directly. Moreover, this property maintains in a wide wavelength range, which originates from the fact that the phase-matching was satisfied at the central region of the coupler for different wavelengths.

3 Simulation results and optimization

The PSR is based on adiabatic mode evolution principle. A finite-difference eigenmode method (FDE) solver (from Lumerical Inc.) is employed to optimize bandwidth of proposed PSR in near infrared region. We sweep the slab layer widths (W_{s1} and W_{s2}) and choose optimal slab width $W_{s1} = 1 \mu\text{m}$, $W_{s2} = 0.35 \mu\text{m}$ to ensure broadband phase-match for input TM_0 mode and crossed TE_0 mode. The etched depth $H_t = 70 \text{ nm}$ is chosen considering the waveguide confinement condition for TM_0 mode in silicon core. Fig. 2(a) shows the effective refractive indices of input TM_0 mode and cross port TE_0 mode as a function of ridge layer shape factor (defined as $f = W_{t1}/W_{s1} = 1 - (W_{t2}/W_{s2})$) which varies from 0 to 1 at six typical wavelengths of 1250, 1350, 1450, 1550, 1650, 1750 nm. The effective refractive indices of TM_0 mode and cross port TE_0 mode become close and cross each other. According to above explanation, such phase-match introduces mode conversion between TM_0 mode and crossed TE_0 mode when light propagates along with the adiabatic taper structure. Thus, the energy carried by

input TM_0 mode can be transferred to crossed TE_0 mode within a suitable coupling length. This is applicable to all the six selected wavelengths. Therefore, it can be inferred that the designed PSR can work in the range of 1250 nm to 1750 nm. On the other hand, Fig.2(b) illustrates n_{eff} of input TE_0 mode as a function of ridge layer shape factor varies from 0 to 1 at above mentioned six typical wavelengths. In each wavelength, the effective refractive index of input TE_0 mode decreases slowly and stays far away from crossed TE_0 mode (the second-highest super-mode). The considerable phase-mismatch prevents mode energy transmission for input TE_0 mode, which allows an input TE_0 mode to pass through the waveguide with slight insertion loss in an ultra-



broadband.

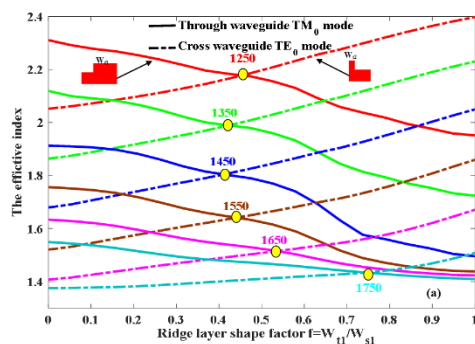


Fig. 2. Calculated effective refractive indices of (a) TE_0 mode and (b) TM_0 mode for right hand side waveguide (input port) in comparison of left hand side waveguide (cross port) TE_0 mode as a function of different ridge taper shape factor, at 1250 nm, 1350 nm, 1450 nm, 1550 nm, 1650 nm, 1750 nm, respectively.

In order to describe the change of polarization state caused by the adiabatic taper coupler, a parameter of mode polarization ratio γ_x is defined as the ratio of the electric field energy in the x -axis to the y -axis, which can determine the polarization state of hybridized mode during the mode evolution process. γ_x can be calculated by [31]:

$$\gamma_x = \frac{\iint |E_x^2| dx dy}{\iint |E_x^2| dx dy + \iint |E_y^2| dx dy} \quad (5)$$

E_x and E_y are eigenmodes electrical field components for the x -axis and y -axis, respectively. A typical TE mode profile is majorly composed of the x -axis component and vice versa. Generally, there is $\gamma_x > 90\%$ for TE mode and $\gamma_x < 10\%$ for TM mode in a regular rectangle waveguide.

Fig. 3 shows the calculated mode polarization ratios γ_x for the super-mode excited by TE_0 and TM_0 input supported in the PSR with the various ridge shape factor, respectively. The wavelength of input light is 1550 nm. The solid orange line illustrates a rapid polarization rotation for TM_0 mode. The γ_x for TM_0 super-mode changed from 4% to 94%. The five insets show the mode profiles at the corresponding yellow points. It is clear that the mode profile changes with the variation of γ_x . On the one hand, the electric field confined by the edges of the waveguide changes from vertical distribution to transverse distribution. On the other hand, the electric field profiles transfer from the wide waveguide (input port) to the narrow waveguide (cross port). On the contrary, the insets corresponding to the green dot shows the input TE_0 mode is confined in the input port. The blue dot-dash line indicates the polarization state of the input TE_0 mode is stable. Thus, an efficient PSR can be achieved through inverse asymmetrical ridge taper structure.

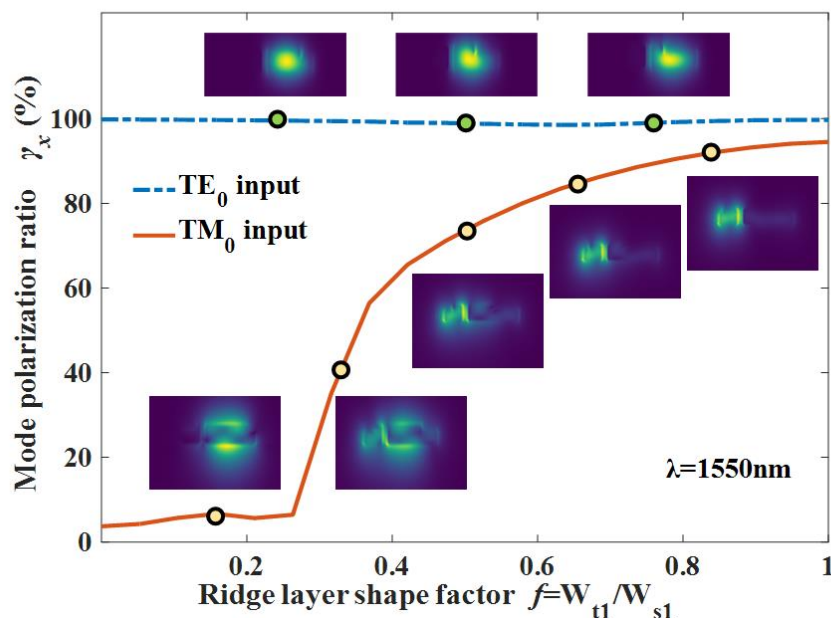


Fig. 3. The calculated mode profiles and polarization ratio γ_x of the super-mode supported in the PSR as a function of different taper waveguide sections in mode propagation.

Coupling length is another critical parameter for the proposed PSR. It will determine coupling efficiency greatly. Therefore, we try to find the optimized coupling length by employing eigenmode expansion (EME) and matching method. To achieve this, the input TM_0 mode polarization conversion efficiencies as functions of wavelength and coupling length are calculated. The results are shown in Fig. 4(a). It should be noted that with the increase of the working wavelength, the coupling length L_c for achieving the highest coupling efficiency is gradually reduced. The optimal value for L_c is chosen to be 520 nm with consideration of maintaining high conversion efficiency in optical fiber communication bands. In addition, etching depth H_t can also influence the conversion efficiency. So the conversion efficiency as functions of

wavelength and the etching depth H_t are analyzed in the same condition with a fixed L_c , the result shown in Fig. 4(b). It suggests that the high polarization conversion efficiency can be maintained at $H_t = 70 \pm 10$ nm. Otherwise, the performance rapidly worsens when H_t is outside this range. According to above analysis, all structural parameters for proposed PSR are optimized and listed in Table 1.

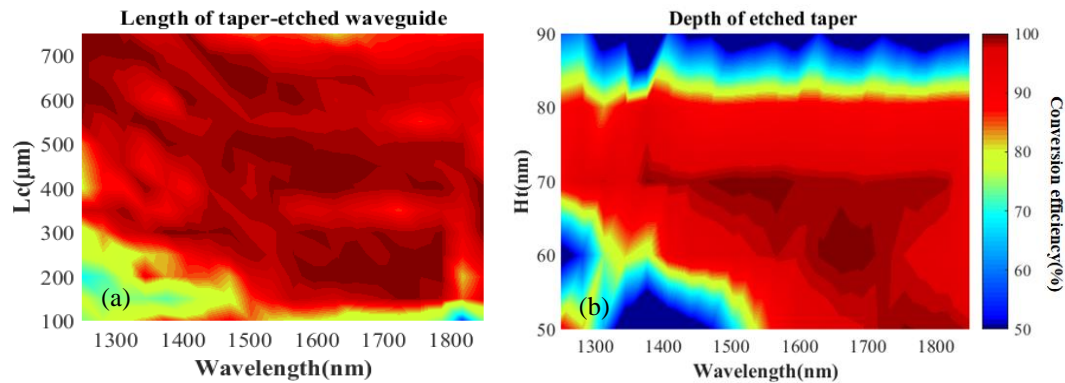


Fig. 4. The calculated polarization conversion efficiency when TM_0 inject as functions of wavelength and structure parameters of (a) L_c and (b) H_t

Table. 1 structural parameters of PSR

| Parameter | Value(μm) | Description |
|-----------|------------------------------------|---|
| W_{s1} | 1 | Width of the input taper-etched waveguide |
| W_{s2} | 0.35 | Width of the cross taper-etched waveguide |
| W_{t1} | Linear gradient from W_{s1} to 0 | Width of the input ridge taper |
| W_{t2} | Linear gradient from 0 to W_{s2} | Width of the cross ridge taper |
| H_t | 0.07 | Depth of etched taper |
| W_g | 0.12 | Width of the gap between two waveguides |
| L_c | 520 | Length of the etched taper |

Fig. 5(a)-(f) shows the field profiles for incident TM_0 mode and TE_0 mode by using EME when PSR operating at wavelength of 1250, 1550, 1750 nm, respectively. It can be seen that the input TM_0 mode gradually converts into the TE_0 modes at the cross port, while the input TE_0 mode passes through the waveguide without mode conversion. The mode field profile is diverse for different wavelength conditions, but the pattern of mode evolution is consistent. In particular, for 1750 nm TM_0 mode, it converts to TE_0 mode in the rear segment instead of the middle segment where 1250 nm and 1550 nm TM_0 mode converted, which is consistent with our above n_{eff} analysis. From another point of view, the field profiles also verified the operation wavelength flexibility of proposed PSR, hence an ultra-broadband PSR with high-efficiency is realized.

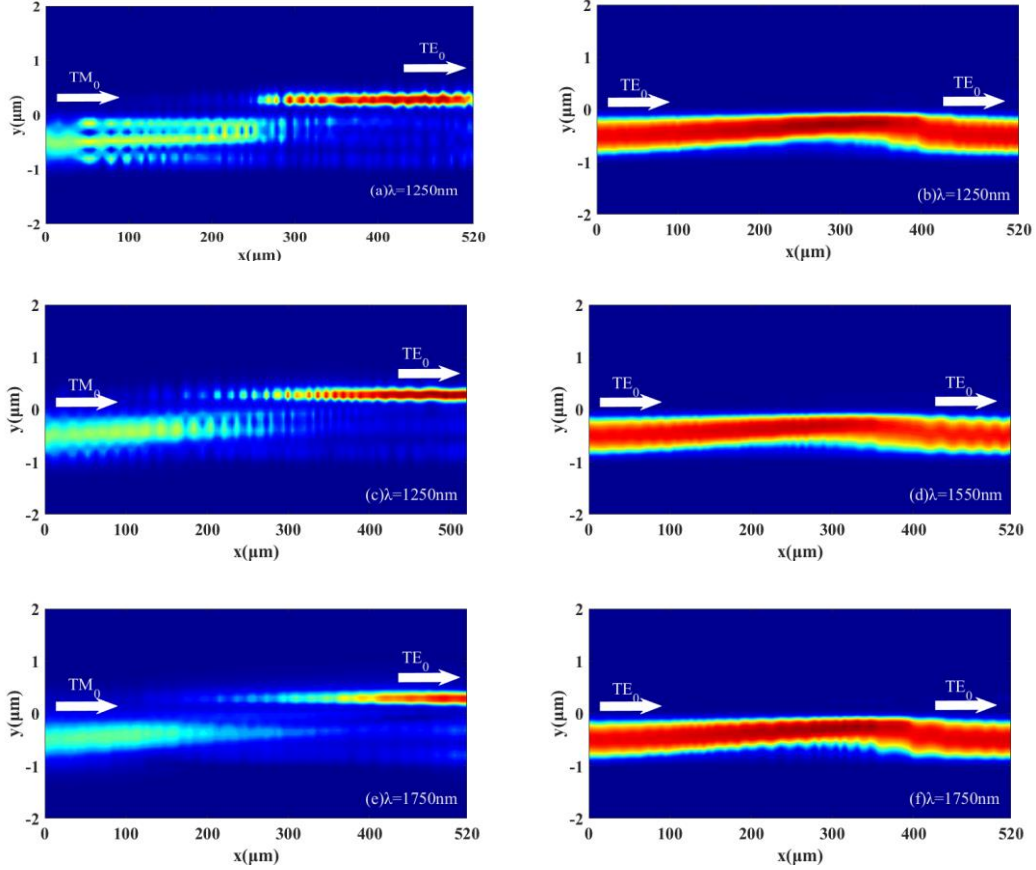


Fig. 5. Magnetic mode profile distribution of (a) 1250 nm TM_0 inject (b) 1250 nm TE_0 inject (c) 1550 nm TM_0 inject (d) 1550 nm TE_0 inject (e) 1750 nm TM_0 inject (f) 1750 nm TE_0 inject

The key figures of merit usually employed for PSR performance are the average insertion loss (IL), crosstalk (CT), and extinction ratio (ER). The IL, CT, and ER for input TE_0 mode, defined as [32]:

$$PER_{TE \text{ to } TE}^{Through} = 10 \times \log_{10} \left(\frac{P_{TE}^{Through}}{P_{TM}^{Through}} \right) \quad (6)$$

$$IL_{TE \text{ to } TE}^{Through} = -10 \times \log_{10} \left(P_{TE}^{Through} \right) \quad (7)$$

$$CT_{TE \text{ to } TE}^{Cross} = 10 \times \log_{10} \left(\frac{P_{TE}^{Cross}}{P_{TE}^{Through}} \right) \quad (8)$$

The IL, CT, and ER for input TM_0 mode are defined as [32]:

$$PER_{TM \text{ to } TE}^{Cross} = 10 \times \log_{10} \left(\frac{P_{TE}^{Cross}}{P_{TM}^{Cross}} \right) \quad (9)$$

$$IL_{TM \text{ to } TE}^{Cross} = -10 \times \log_{10} \left(P_{TE}^{Cross} \right) \quad (10)$$

$$CT_{TM \text{ to } TE}^{Cross} = 10 \times \log_{10} \left(\frac{P_{TM}^{Through}}{P_{TE}^{Cross}} \right) \quad (11)$$

The three-dimensional finite-difference time-domain (3-D FDTD) method is implemented to verify the performance of the proposed PSR. Fig. 6(a) shows the transmission spectra (1200 -1800 nm) of TM_0 and TE_0 mode at cross and through port when the TE_0 is launched, respectively. As the figure shows, the transmissions are wavelength-insensitive and most of the energy output at through port is in the form of TE_0 . The ILs for input TE_0 mode within the entire wavelength range are below 0.05 dB. In contrast, the output fields of TM_0 at through port, TM_0/TE_0 at cross port are all small.

The corresponding PER is better than 60 dB, the CT is lower than -60 dB. The extremely low IL is clear evidence of the input TE₀ mode not affected by the coupler and being restricted to transmit along the waveguide. The transmission spectra of the device with TM₀ mode inputs at through port and cross port are plotted in Fig. 6(b). It can be seen in Fig. 6(b) the ILs for input TE₀ mode in 1250 nm to 1750 nm wavelength range is below 0.2 dB, while the PERs in this range are better than 15 dB, the CTs is lower than -30 dB.

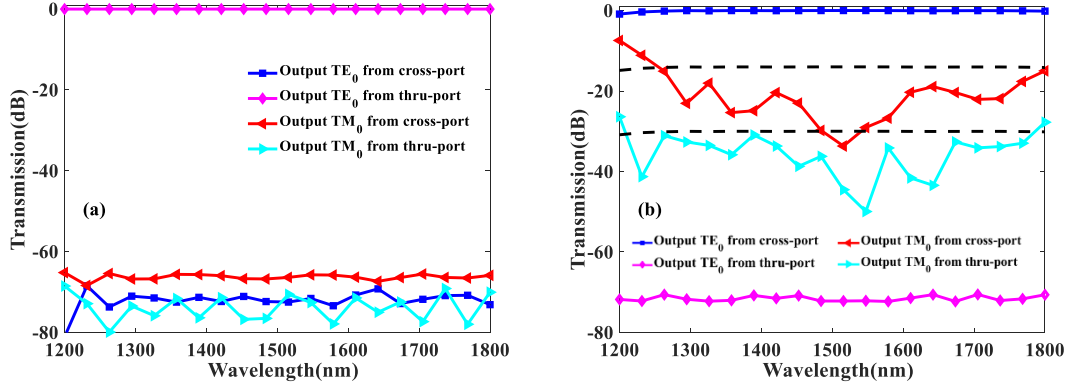
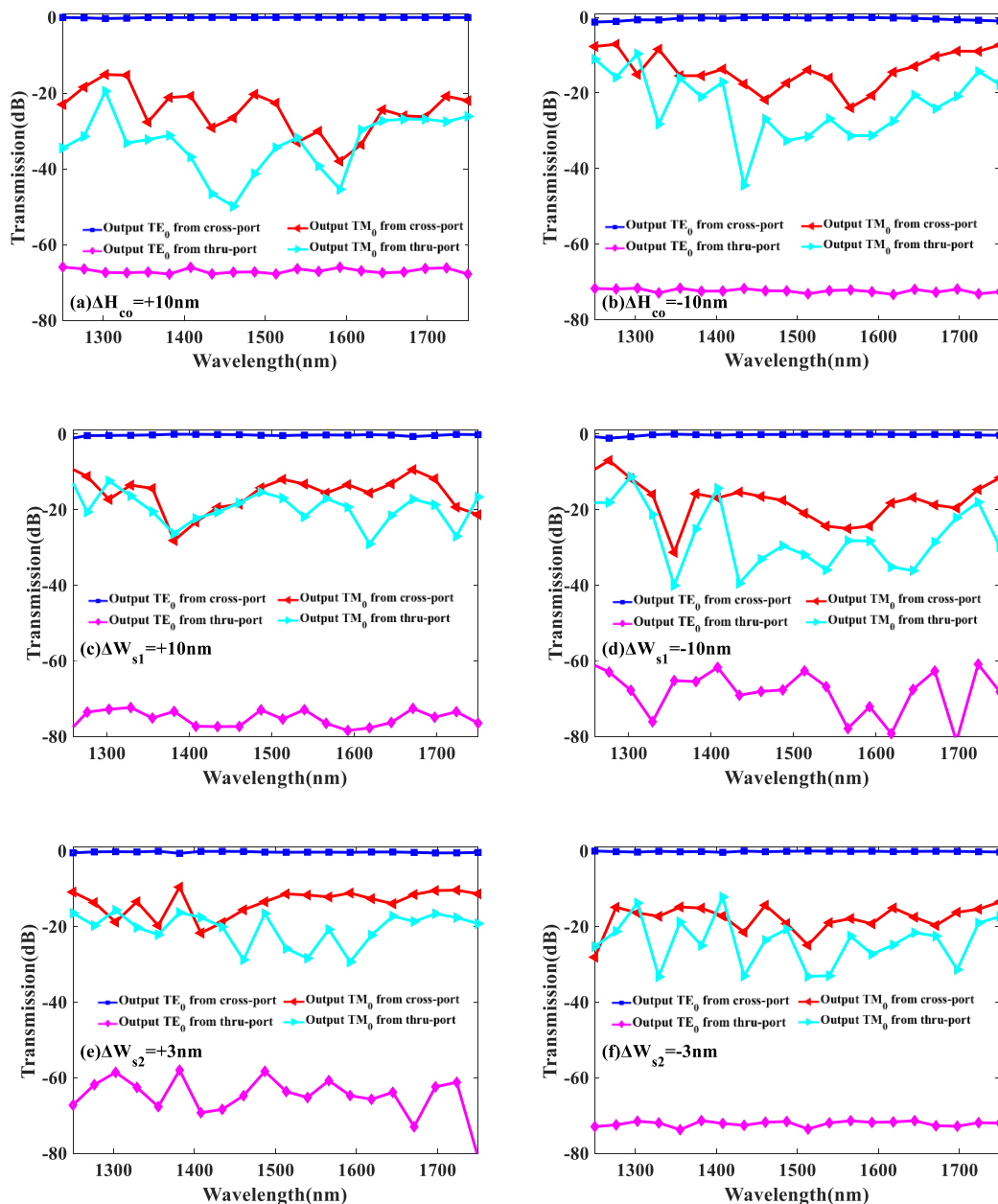


Fig. 6. Transmission of designed PSR as a function of wavelength dependence when injecting: (a) TE₀ mode and (b) TM₀ mode

Fabrication errors such as inaccuracy and misalignment are inevitable in current lithography technology. From an engineering application perspective, it is necessary to perform tolerance analysis, since the fabrication tolerance for input TE₀ mode is very large due to strong waveguide confinement. For simplicity, the fabrication tolerance analysis is performed only for input TM₀ mode in the following. There are five types of fabrication errors introduced during the lithography process: the coupling length error ΔL_c , the waveguide slab width error ΔW_{s1} and ΔW_{s2} , the total height error ΔH_{co} , and the etched depth error ΔH_t . Tolerances analysis for each type of error is carried out individually, while keeping the other parameters at optimal values. According to Fig. 4 (a), the conversion efficiency is insensitive to ΔL_c , so the tolerance of L_c is large enough to be negligible. For two waveguide slab width error ΔW_{s1} and ΔW_{s2} , the linewidth nonuniformity is usually less than 1% for standard 193 nm lithography [34]. Thus, ΔW_{s1} and ΔW_{s2} are set to $\pm 1\%$ of the optimal value accordingly (i.e. $\Delta W_{s1} = \pm 10$ nm, $\Delta W_{s2} = \pm 3$ nm). On the other hand, based on previous fabrication experience [29], height deviation ΔH_{co} and ΔH_t are set to ± 10 nm in our analysis.

The results are shown in Figs. 7(a)-(h). Polarization conversion efficiency >91% (IL < 0.4 dB) is taken as criteria for defining operating wavelength range. The calculated transmission spectra for the wafer thickness deviation $\Delta H_{co} = +10$ nm and -10 nm cases are shown in Fig. 7(a)-(b), respectively. The results suggest that the operating wavelength range of 1270-1720 nm is obtained, and PER > 11 dB, CT < -15 dB is maintained in this bandwidth. Fig. 7(c)-(d) describe the transmission spectra when input waveguide width deviation of $\Delta W_{s1} = +10$ nm and -10 nm, respectively. It can be seen that the operating wavelength range is 1310-1690 nm, and PER > 13 dB, CT < -15 dB in this bandwidth. Fig. 7(e)-(f) show transmission spectra when the cross port waveguide width deviation of $\Delta W_{s2} = +3$ and -3 nm, respectively. The results show that the operating wavelength range of 1270-1690 nm, PER > 12 dB, and CT < -14 dB are

achieved within the bandwidth. Transmission spectra for etched depth deviation of $\Delta H_t = +10$ nm and -10 nm is shown in Fig. 7(g)–(h), respectively. The results show that the operating wavelength range of 1250–1750 nm, PER > 15 dB, and CT < -25 dB are achieved within the bandwidth. These results indicate that the proposed PSR within the maximum acceptable fabrication error achieves IL < 0.4 dB for 380 nm bandwidth (1310 nm–1690 nm). Table 2 summarizes several reported on-chip PSRs and compare them with our proposed structure. It shows that our work has high polarization conversion efficiency, low crosstalk, and broadest operating bandwidth, which is favorable for high-performance PICs.



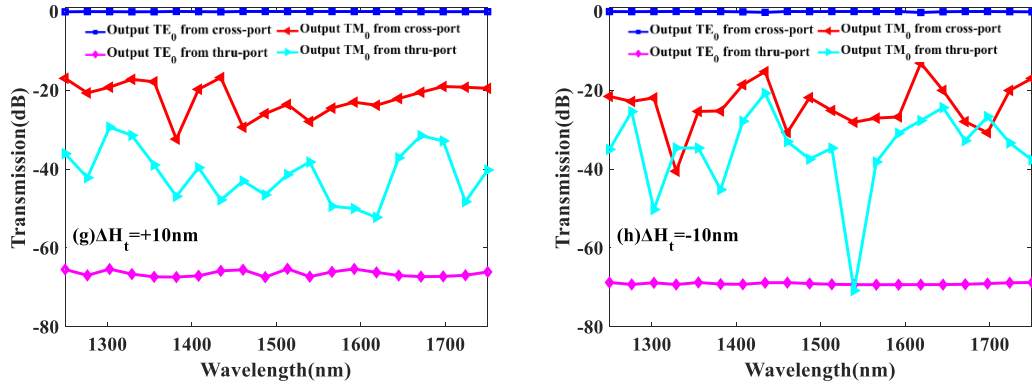


Fig. 7. Wavelength dependence of the designed PSR when (a) $\Delta h_{co} = 10$ nm, and (b) -10 nm (c) $\Delta w_{s1} = 10$ nm, and (d) -10 nm. (e) $\Delta w_{s2} = 3$ nm, and (f) -3 nm (g) $\Delta h_t = 10$ nm, and (h) -10 nm when input TM_0 mode.

Table.2 Comparison of several SOI PSR

| Structures | Crosstalk | Insertion loss | Bandwidth |
|--------------------------------------|-----------|----------------|-----------|
| | (dB) | (dB) | (nm) |
| Asymmetrical Directional Coupler[14] | - | 0.6 | 35 |
| Bend Waveguides[16] | -18 | 0.3 | 70 |
| Bend Waveguides[17] | -19 | 0.11 | 100 |
| SWG Directional Coupler[19] | -14 | 0.4 | 35 |
| Taper with ADC[21] | -35 | ~0.4 | 50 |
| Taper with SWG-assisted ADC[24] | -19 | 1.4 | 120 |
| Asymmetric Y-junction[26] | -13 | 0.4 | 400 |
| Taper with MMI[27] | -15 | 0.5 | 50 |
| Taper with MMI[28] | - | 0.86 | 50 |
| Bi-level taper with ADC [29] | - | 0.18 | 300 |
| Bi-level taper - STA coupler[30] | -20 | 1 | 100 |
| MMI[32] | -25 | 1 | 40 |
| This work | -30 | 0.2 | 500 |

4 Conclusion

In summary, a novel PSR based on mode evolution by using inverse asymmetrical ridge taper coupler is proposed. The structural parameters are optimized according to the phase-matching condition in the mode hybridization regions. The performance of proposed PSR is systematically analyzed. For input TE_0 mode, the IL is exceedingly low (< 0.05 dB), and PER and CT are better than 60 dB and -60 dB, respectively. For input TM_0 mode, the IL is less than 0.2 dB, the PER and the CT is better than 15 dB and -30 dB, respectively. The polarization conversion efficiency is 95% over bandwidth of 500 nm (from 1250 nm to 1750 nm). Furthermore, fabrication-tolerant analysis indicates that the designed PSR keeps high polarization conversion efficiency ($> 91\%$) in 380 nm wavelength range (1310 nm-1690 nm) within 1% fabrication deviation.

Compared with previously reported PSR, the proposed on-chip PSR has a broader bandwidth covering all optical fiber communication waveband (from O to U band) for the first time to the best of our knowledge. The proposed PSR is fully CMOS-compatible and will find potential applications in large scale/high performance PICs.

Acknowledgments

This work is supported by the National Nature Science Fund of China (No: 61875165, 61775180, 61772417), the Shaanxi International Science and Technology Cooperation & Exchange Program (No: 2017KW-027), Collaborative Innovation Project of Shaanxi Provincial Department of Education (No: 20JY060), and the New Star Team of Xi'an University of Posts & Telecommunications (2016).

Reference:

1. R. Soref, "The past, present, and future of silicon photonics," *IEEE J. Sel. Top. Quantum Electron.* **12**(6), 1678–1687 (2006).
2. T. Barwicz, M. R. Watts, M. A. Popovi, P. T. Rakich, L. Socci, F. X. Kärtner, E. P. Ippen, and H. I. Smith, "Polarization-transparent microphotonic devices in the strong confinement limit," *Nat. Photonics* **1**(1), 57–60 (2007).
3. C. Manolatou, S. G. Johnson, S. Fan, P. R. Villeneuve, H. A. Haus, and J. D. Joannopoulos, "High-Density Integrated Optics," **17**(9), 1682–1692 (1999).
4. C.-W. Hsu, H.-Y. Lin, J.-Y. Chen, and Y.-C. Cheng, "Ultra-compact polarization rotator in an asymmetric single dielectric loaded rib waveguide," *Appl. Opt.* **55**(6), 1395 (2016).
5. E. J. Stanton, L. Chang, W. Xie, A. Malik, J. Peters, J. Chiles, N. Nader, G. Navickaite, D. Sacchetto, M. Zervas, K. Srinivasan, J. E. Bowers, S. B. Papp, S. W. Nam, and R. P. Mirin, "On-chip polarization rotator for type i second harmonic generation," *APL Photonics* **4**(12), 126105 (2019).
6. J. Fan, C. Huang, and L. Zhu, "A compact, broadband slot waveguide polarization rotator," *AIP Adv.* **1**(4), 042136 (2011).
7. L. Gao, Y. Huo, J. S. Harris, and Z. Zhou, "Ultra-compact and low-loss polarization rotator based on asymmetric hybrid plasmonic waveguide," *IEEE Photonics Technol. Lett.* **25**(21), 2081–2084 (2013).
8. H. Xu and Y. Shi, "Subwavelength-grating-assisted silicon polarization rotator covering all optical communication bands," *Opt. Express* **27**(4), 5588 (2019).
9. J. M. Hong, H. H. Ryu, S. R. Park, J. W. Jeong, S. G. Lee, E. H. Lee, S. G. Park, D. Woo, S. Kim, and O. Beom-Hoan, "Design and fabrication of a significantly shortened multimode interference coupler for polarization splitter application," *IEEE Photonics Technol. Lett.* **15**(1), 72–74 (2003).
10. D. Dai and J. E. Bowers, "Ultrashort and ultrabroadband silicon polarization beam splitter based on a bent directional coupler," *Opt. InfoBase Conf. Pap.*

- 19**(19), 1286–1288 (2011).
11. S. Lin, J. Hu, and K. B. Crozier, "Ultracompact, broadband slot waveguide polarization splitter," *Appl. Phys. Lett.* **98**(15), 98–100 (2011).
 12. D. Chen, X. Xiao, L. Wang, G. Gao, W. Liu, and Q. Yang, "Broadband, Fabrication-Tolerant Polarization Beam Splitters Based on a Tapered Directional Coupler," *IEEE Photonics Technol. Lett.* **28**(19), 2074–2077 (2016).
 13. Y. Tian, J. Qiu, C. Liu, S. Tian, Z. Huang, and J. Wu, "Compact polarization beam splitter with a high extinction ratio over S + C + L band," *Opt. Express* **27**(2), 999 (2019).
 14. L. Liu, Y. Ding, K. Yvind, and J. M. Hvam, "Silicon-on-insulator polarization splitting and rotating device for polarization diversity circuits," *Opt. Express* **19**(13), 12646 (2011).
 15. H. Guan, A. Novack, M. Streshinsky, R. Shi, Q. Fang, A. E.-J. Lim, G.-Q. Lo, T. Baehr-Jones, and M. Hochberg, "CMOS-compatible highly efficient polarization splitter and rotator based on a double-etched directional coupler," *Opt. Express* **22**(3), 2489 (2014).
 16. Y. Zhang, Y. He, X. Jiang, B. Liu, C. Qiu, Y. Su, and R. A. Soref, "Ultra-compact and highly efficient silicon polarization splitter and rotator," *APL Photonics* **1**(9), 091304 (2016).
 17. K. Tan, Y. Huang, G.-Q. Lo, C. Lee, and C. Yu, "Compact highly-efficient polarization splitter and rotator based on 90° bends," *Opt. Express* **24**(13), 14506 (2016).
 18. K. Tan, Y. Huang, G.-Q. Lo, C. Yu, and C. Lee, "Experimental realization of an O-band compact polarization splitter and rotator," *Opt. Express* **25**(4), 3234 (2017).
 19. Y. Xiong, J. G. Wangüemert-Pérez, D.-X. Xu, J. H. Schmid, P. Cheben, and W. N. Ye, "Polarization splitter and rotator with subwavelength grating for enhanced fabrication tolerance," *Opt. Lett.* **39**(24), 6931 (2014).
 20. L. Liu, Q. Deng, and Z. Zhou, "Manipulation of beat length and wavelength dependence of a polarization beam splitter using a subwavelength grating," *Opt. Lett.* **41**(21), 5126 (2016).
 21. D. Dai and J. E. Bowers, "Novel concept for ultracompact polarization splitter-rotator based on silicon nanowires," *Opt. Express* **19**(11), 10940 (2011).
 22. X. Tu, M. Li, J. Xing, H. Fu, and D. Geng, "Compact PSR Based on an Asymmetric Bi-level Lateral Taper in an Adiabatic Directional Coupler," *J. Light. Technol.* **34**(3), 985–991 (2016).
 23. Y. Zhao, C. Qiu, A. Wu, H. Huang, J. Li, Z. Sheng, W. Li, X. Wang, and F. Gan, "Broadband polarization splitter-rotator and the application in WDM receiver," *IEEE Photonics J.* **11**(1), 1–10 (2019).
 24. M. Ma, A. H. K. Park, Y. Wang, H. Shoman, F. Zhang, N. A. F. Jaeger, and L. Chrostowski, "Sub-wavelength grating-assisted polarization splitter-rotators for

- silicon-on-insulator platforms," *Opt. Express* **28**(11), 17122 (2020).
25. S. Keyvaninia, H. Boerma, M. Wössner, F. Ganzer, P. Runge, and M. Schell, "Highly efficient passive InP polarization rotator-splitter," *Opt. Express* **27**(18), 25872 (2019).
 26. J. Wang, B. Niu, Z. Sheng, A. Wu, W. Li, X. Wang, S. Zou, M. Qi, and F. Gan, "Novel ultra-broadband polarization splitter-rotator based on mode-evolution tapers and a mode-sorting asymmetric Y-junction," *Opt. Express* **22**(11), 13565–13571 (2014).
 27. D. Dai and H. Wu, "Realization of a compact polarization splitter-rotator on silicon," *Opt. Lett.* **41**(10), 2346 (2016).
 28. H. Xu and Y. Shi, "Ultra-compact and highly efficient polarization rotator utilizing multi-mode waveguides," *Opt. Lett.* **42**(4), 771 (2017).
 29. Y. Yin, Z. Li, and D. Dai, "Ultra-Broadband Polarization Splitter-Rotator Based on the Mode Evolution in a Dual-Core Adiabatic Taper," *J. Light. Technol.* **35**(11), 2227–2233 (2017).
 30. D. Guo and T. Chu, "Broadband and low-crosstalk polarization splitter-rotator with optimized tapers," *OSA Contin.* **1**(3), 841 (2018).
 31. S. Keyvaninia, H. Boerma, M. Wössner, F. Ganzer, P. Runge, and M. Schell, "Highly efficient passive InP polarization rotator-splitter," *Opt. Express* **27**(18), 25872 (2019).
 32. Y. Liu, S. Wang, Y. Wang, W. Liu, H. Xie, Y. Yao, Q. Song, X. Zhang, Y. Yu, and K. Xu, "Subwavelength polarization splitter – rotator with ultra-compact footprint," *Opt. Lett.* **44**(18), 4495–4498 (2019).
 33. A. Yariv, P. Yeh, *Photonics: Optical Electronics in Modern Communications (the Oxford Series in Electrical and Computer Engineering)* (2006).
 34. S. K. Selvaraja, W. Bogaerts, P. Dumon, D. Van Thourhout, and R. Baets, "Subnanometer linewidth uniformity in silicon nanophotonic waveguide devices using CMOS fabrication technology," *IEEE J. Sel. Top. Quantum Electron.* **16**(1), 316–324 (2010).